MDPI

Article

Derived Profiles of CCN and INP Number Concentrations in the Taklimakan Desert via Combined Polarization Lidar, Sun-Photometer, and Radiosonde Observations

Shuang Zhang [1], Zhongwei Huang [1,2,*], Khan Alam [1,3], Meishi Li [1], Qingqing Dong [1], Yongkai Wang [1], Xingtai Shen [1], Jianrong Bi [1], Jiantao Zhang [4], Wuren Li [1], Ze Li [1], Wenbiao Wang [5], Zhengnan Cui [5] and Xiaodong Song [1]

1   Collaborative Innovation Center for West Ecological Safety (CIWES), Key Laboratory for Semi-Arid Climate Change of the Ministry of Education, College of Atmospheric Sciences, Lanzhou University, Lanzhou 730000, China
2   Collaborative Innovation Center on Forecast and Evaluation of Meteorological Disasters (CIC-FEMD), Nanjing University of Information Science & Technology, Nanjing 210044, China
3   Department of Physics, University of Peshawar, Peshawar 25120, Khyber Pakhtunkhwa, Pakistan
4   Institute of Desert Meteorology, China Meteorological Administration/National Observation and Research Station of Desert Meteorology, Taklimakan Desert of Xinjiang, Urumqi 830002, China
5   Elion Resources Group Co., Ltd., No.15 Guanghua Road, Chaoyang District, Beijing 100026, China
*   Correspondence: huangzhongwei@lzu.edu.cn

Abstract: Understanding the vertical structures of cloud condensation nuclei (CCN) and ice-nucleating particle (INP) number concentrations in desert source regions is crucial for examining dust-cloud interactions and other related impacts. To explore the vertical profiles of the CCN and INP number concentrations and their possible atmospheric–dynamic influence factors at the center of the Taklimakan Desert, intensive observations were conducted by employing a ground-based polarization Raman lidar, sounding balloons, and a sun photometer in Tazhong (83.39° E, 38.58° N, 1103 m above sea level) during the summer of 2019. Based on the GRASP algorithm, the extinction-to-volume conversion factor of dust aerosols was 0.85×10^{-12} Mmm^3 m^{-3}, and the extinction-to-number conversion factor was predicted to be 0.20 Mm cm^{-3} on the basis of the sun photometer observations. Thus, the vertical CCN and INP number concentration profiles obtained with different parameterization schemes in the presence of various pollution levels were calculated by combining dust extinction coefficients retrieved by lidar and meteorological data observed by sounding balloon observations. The achieved results indicated that the CCN number concentration varied from 10^{-2} to 10^2 cm^{-3} and decreased from ground level to 12 km with an average value of 36.57 cm^{-3} at the 10–12 km height range, while the INP number concentration based on parameterization schemes D10 and D15 mainly varied from 10^{-1} to 10^2 L^{-1} and from 1 L^{-1} to 10^3 L^{-1}, with average values of 3.50 L^{-1} and 7.80 L^{-1}, respectively. Moreover, we observed a strong relationship between the INP number concentration of scheme D10 and the wind speed, with an R^2 value of 0.72, but a weak relationship between the CCN number concentration and the relative humidity in the boundary layer, with a Spearman's rank correlation coefficient R^2 value of 0.38. The present study provides original and valuable information regarding the CCN and INP number concentrations and their related influencing factors at the center of the Taklimakan Desert and can improve our understanding of the vertical distributions of dust–cloud–atmosphere dynamic interactions, as well as of the roles of dust aerosols in the desert hydrological cycle.

Keywords: Taklimakan desert; cloud condensation nuclei (CCN); ice-nucleating particle (INP); extinction-to-volume conversion; extinction-to-number conversion factor; lidar measurements

1. Introduction

The Taklimakan Desert has a relatively large impact on climate change in coastal East Asia, as it participates in precipitation involving both water and ice nuclei [1]. According to the mineralogical composition of dust, when dust from anthropogenic sources covers soluble substances, it can lead to the quasideactivation of the ice cores of natural dust [2]. Kelly et al. (2007) showed that a small amount of highly soluble elements significantly enhanced the ability of fine dust particles to act as cloud condensation nuclei (CCN) [3]; these particles strongly compete for water vapor in the nucleation region of the cloudy updraft, thus potentially lessening cloud droplet formation [4]. The concentration of CCN in dusty areas is reduced by 10–20% due to the competition of sand and dust for condensable H_2SO_4, thus reducing the condensation growth of ultrafine model particles to the CCN scale [5]. Manktelow et al. (2010) found that, in an extreme dust event occurring in Japan, South Korea, and eastern China, the average CCN particle size decreased by less than 5% because of the reduction in fine particles being compensated by the growth of coarse dust particles [6]. In addition, CCN number concentrations exhibited strong seasonality, with higher number concentrations observed in winter and lower number concentrations observed in summer under all water supersaturation (SS) conditions; hygroscopicity is generally high in early autumn and low in early summer in Tsukuba, Japan [7].

Desert dust [8] and local basaltic dust mixed with marine aerosols [9]; bioaerosols in the forms of (but not limited to) pollens, viruses, fungal spores, bacteria, and plant debris [10]; seaspray aerosols [11]; elevated plumes [12]; airborne dust from retreating glaciers [13]; black carbon [14]; and salts [15] can all serve as sources of primary ice-nucleating particles (INPs) and CCN, which in turn lead to high INP and CCN number concentrations, which are influenced by both snow-free terrestrial and marine sources [16]. When CCN are dominated by dust particles, alterations occur in the ice cloud particle size and concentration, which lead to the initiation of drizzle and precipitation by forming effective collector drops [17]. When CCN are dominated by dust particles, a near tripling of CCN not dominated by dust are associated with twice the aerosol optical depth (AOD) [18]. Over the Asian monsoon region, synergistic HNO_3–H_2SO_4–NH_3 CCN are also highly efficient INPs that are comparable to desert dust in the upper troposphere [19].

The relative position and concentration of ice nuclei have various effects on the precipitation and atmospheric environment subjected to different pollution levels. The atmospheric concentrations of INPs and CCN in frontal-cloud case tests performed with explicit microphysical models demonstrated substantial sensitivities of the cloud- and ice-water paths, the surface precipitation rate, and the average ice number concentration [20]. Very large CCN result in the early development of large drops in relatively low cloud regions when the background concentration of small nuclei is high [21]. The variations in very large CCN concentrations were found to remarkably influence the surface precipitation of spring hailstorms and storm microphysical processes in the semiarid region examined by the Regional Atmospheric Modeling System [22]. Large-scale weather systems and violent local thermal circulation can form local precipitation in deserts [23]. Commonly, precipitation influenced by INPs and CCN [1] significantly affects shrub vegetation [24], the carbon sequestration capacity [25], the spatial distribution [26], and the microbial beta diversity and community composition of deserts [27]. Desert species and the resources they provide, such as intense pulses and infrequent precipitation, make it possible for such ecosystems to be resilient to climate change [28]. The evaporation of mega dune surfaces after extreme precipitation events is negatively influenced and requires a long time for complete removal [29].

The complexity of atmospheric aerosols [30], the inaccurate representation of the INP [31], and instrument discrepancies [32] cause large parameterization uncertainties in atmospheric models, resulting in large deficiencies in cloud and precipitation predictions. To improve the application of aerosol-dependent INP number concentrations in climate models [33], the vertical profiles of the CCN and INP number concentrations were retrieved in this study under three pollution levels by utilizing a simple CCN parameterization and

available INP parameterization schemes [34]. This paper is structured as follows: Section 2 introduces the data and methods; the results and discussion are given in Section 3; and Section 4 summarizes the paper.

2. Measurements and Methods

To obtain reliable vertical structures of the CCN and INP number concentrations in the desert, we conducted intensive observations in the summer of 2019 at Tazhong (83.39° E, 38.58° N, 1103 m above sea level), which is located in the hinterland of the Taklimakan Desert. Three main instruments were employed for the observations in this study, as are shown in Figure 1. A high-spatiotemporal-resolution polarization lidar, designed for lidar network observations, was used to investigate the profiles of dust extinction coefficients. A sun photometer was used to observe the dust optical thickness at different wavelengths to invert the spectral distribution of the number concentration and volume concentration of dust aerosols using the GRASP algorithm. Moreover, radio sounding was used to obtain profiles of air pressure and temperature as model inputs to calculated the INC number concentration in the atmosphere and discuss its correlation with wind speed. Profiles of CCN and INP concentration were derived based on Mamouri and Ansmann (2016) [35].
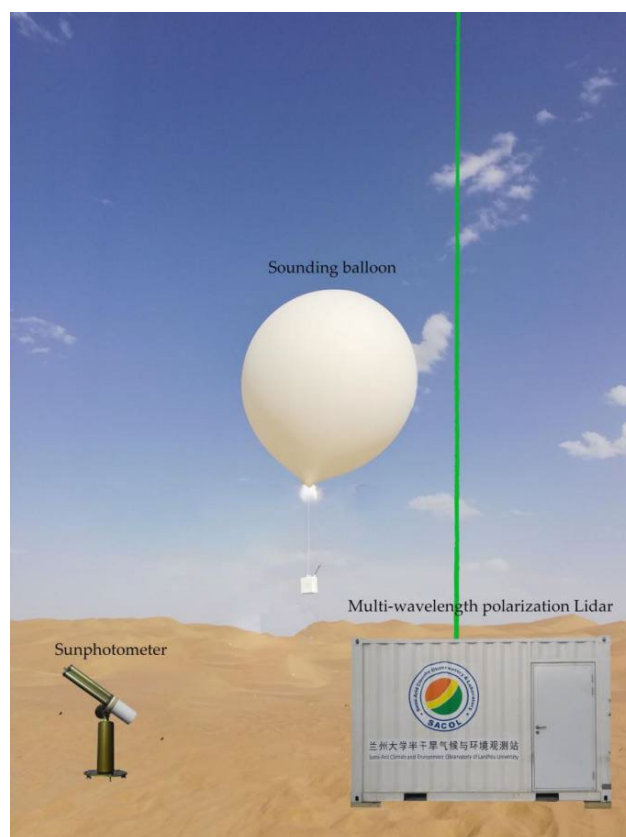
Figure 1. Three instruments, including a sun photometer, polarization lidar, and sounding balloon, were employed during an intensive observation period (IOP) in the center of the Taklimakan Desert in the summer of 2019.

2.1. Polarization Lidar Measurements

The lidar system consisted of a transmitting system and a receiving system. The transmitting system included an Nd:YAG (neodymium-doped yttrium aluminum garnet) laser emitting a 1064 nm laser and double- and triple-frequency amplifiers to amplify the 1064 nm lasers to 532 nm and 355 nm lasers, respectively. A telescope was used to receive the laser scatter from the atmosphere. Polarization measurements at 532 nm and 355 nm, nitrogen Raman signals at 387 nm and 607 nm, and a water vapor Raman signal at 407 nm

were collected. In addition, a Mie scattering signal at 1064 nm was also observed. Main detailed information on the Raman–polarization lidar system is shown in Table 1, and the corresponding data-processing methods can be found in our previous studies [36].

Table 1. Polarization lidar parameters.

Parameters	Values
Transmitter	Nd: YAG laser
Repetition rate	10 HZ
Pulse energy	450 mJ
Wavelength	1064 nm, 532 nm and 355 nm
Vertical resolution	3.75 m
Field of view	2 mrad

2.2. Sun Photometer Observations

The sun photometer was placed on a 3.5-meter-high roof at a distance of approximately 10 m from the lidar to detect the dust optical thickness at wavelengths of 1640, 1064, 1020, 940, 870, 670, 550, 532, 527, 500, 440, 380, and 340 nm with an Ångström exponent range of 470–870. Thus, aerosol microphysical properties were further retrieved from sun photometer observations in Tazhong in this study.

2.3. Radiosonde Sounding Data

The radiosonde sounding data were collected from July 26 to July 30, 2019. For this purpose, a sounding balloon was released four times a day at Caimen (83.62° E, 39.03° N) approximately 7 km away from the lidar. The sounding balloons carried detectors such as temperature, pressure, humidity, wind, and global positioning system sensors and provided profiles of temperature, pressure, humidity, wind, and height, respectively, at a temporal resolution of 1 s and a vertical resolution of 10 m. The rising speed of the sounding balloon was in the range of 4.5–6.5 m/s, so the profiles of these parameters with a temporal resolution of 1 s were chosen to perform linear interpolations of the atmospheric temperature and pressure. The final aim was to provide temperature and pressure profiles based on the needs of the lidar vertical resolution.

2.4. Retrieval Methods

The observed lidar data had a temporal resolution of 3 min, while the sun photometer data were not a continuous time series and had a temporal resolution greater than 3 min. Hence, the effective observations of the lidar and solar photometer sensors were defined by the measurement time discrepancy between the lidar and sun photometer being less than 3 min. The sun photometer AOD was employed as an input to retrieve the column volume concentration and effective radius of both the fine and coarse modes using the GRASP algorithm (https://www.grasp-open.com/, (accessed on 17 December 2022)) [37]; the real part of the negative refraction index of sand dust was set as 1.141, and the imaginary part was set as 0.0036 [38]. The lognormal distribution of the column particle number concentration (N) corresponding to each effective observation has the following relationship with the lognormal distribution of volume concentration (V), which is described as follows [39]:

$$R_g^V = R_g^N \exp^{[3(In\delta)^2]},$$

(1)

$$V_0 = N_0 \frac{4}{3} \pi (R_g^N)^3 \exp^{[\frac{9}{2}(In\delta)^2]},$$

(2)

where R_g^V and R_g^N represent the geometric mean volume concentration radius and number concentration radius, respectively, $In\delta$ denotes the spectrum of the lognormal distribution, V_0 is the total volume concentration, and N_0 is the total number concentration. The typical AOD distribution in terms of the wavelength, as well as the variations in V and N as a function of the radius of floating dust as measured by manual recording, are presented

in Figure 2. These results were appropriately tested by ground-based polarization lidar observations taken on 27 July 2019 at 12:06:55 CST.

27-Jul-2019 12:06:55
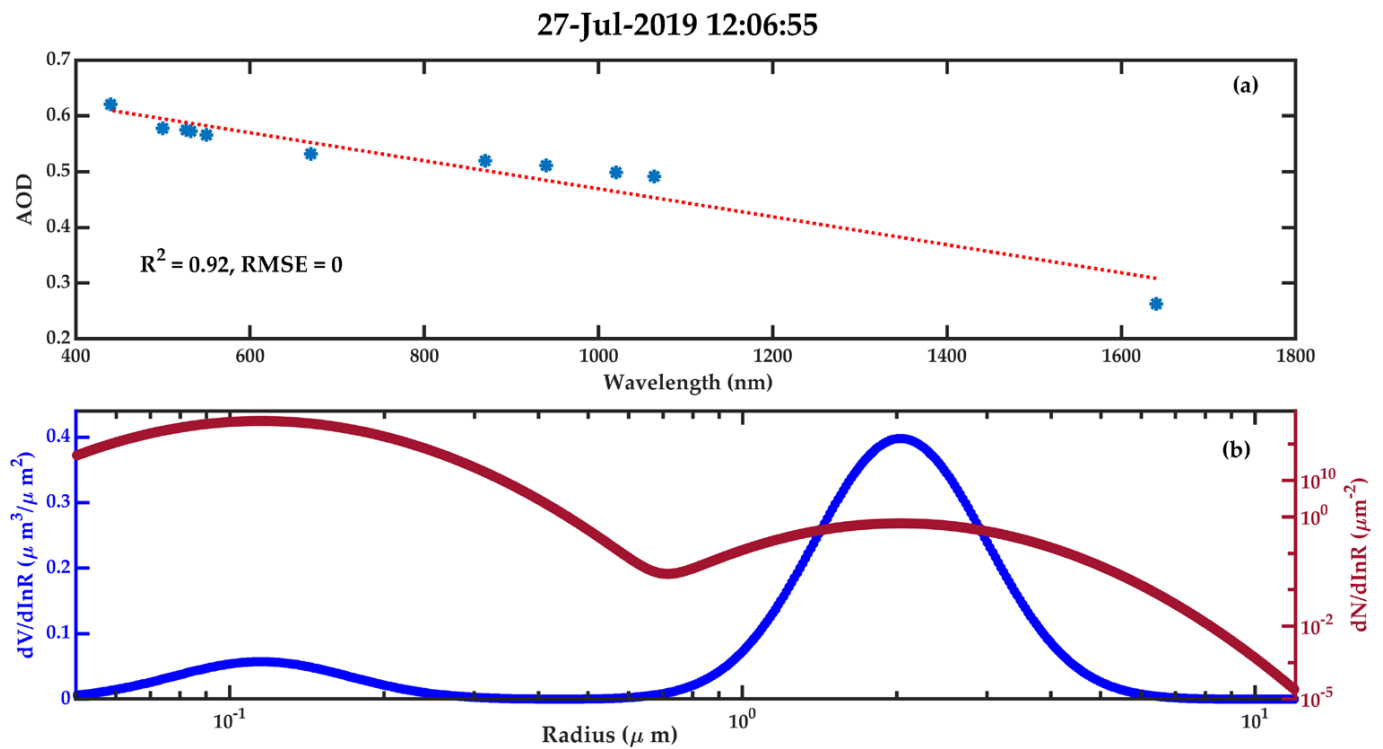
Figure 2. (**a**) Plot of the AODs at eleven wavelengths (i.e., 1640, 1064, 1020, 940, 870, 670, 550, 532, 527, 500, and 440 nm) and (**b**) the column-integrated particle volume size distribution (blue) and particle number size distribution (red) derived from sun photometer observations taken at Tazhong on 27 July 2019 at12:06:55 (CST) via the GRASP–AOD algorithm during a floating dust event.

The dust extinction to column V conversion factor ($c_{v,d}$) and the dust extinction to column N conversion factor ($c_{N,d}$) were evaluated by utilizing Equations (3) and (4) combined with the column volume concentration distributions retrieved from the AODs detected via the sun photometer and assuming the atmospheric column depth (D) to be 1000 m [35], as defined by the following:

$$c_{v,d} = \frac{V_d}{AOD} = \frac{V_d/D}{AOD/D} = \frac{v_d}{\sigma_{d,z}}, \tag{3}$$

$$c_{250,d} = \frac{N_{250,d,dry}}{AOD} = \frac{N_{250,d,dry}/D}{AOD/D} = \frac{n_{250,d,z}}{\sigma_{d,z}}, \tag{4}$$

$$c_{100,d,dry} = \frac{n_{100,d,z}}{\sigma_{d,z} x_d}, \tag{5}$$

where V_d (unit: $\mu m^3/\mu m^2$) and AOD are the dust column volume concentrations and extinction coefficient of the whole atmosphere, respectively, and $N_{d,dry,z}$ is the dust column number concentration with a dry condition at height z in $\mu g\ m^{-3}$. Dust was assumed to be hydrophobic [40] without hygroscopic growth, $N_{250,d,dry} = N_{250,d}$. $n_{250,d,z}$ is the dust number concentration with a dry radius of more than 250 nm at height z. $\sigma_{d,z}$ denotes the dust extinction coefficient at height z in Mm^{-1} retrieved by ground-based polarization lidar based on the Fernald method [41] by assuming the lidar ratio of dust is 49 sr according to Ref. [36] and assuming that the non-dust particles at the cloud height are only cloud particles. $n_{100,d,z}$ is the dust number concentration with a dry radius of more than 100 nm at height z, and x_d is the dust extinction exponent.

The INP number concentration at a height of z was evaluated using the atmospheric pressure and T profiles obtained from the sounding balloons in the formula presented in Table 1, as given in Ref. [42]. For numerical modeling purposes, mineral dust particles from Asian regions could be parameterized as a common particle type [43]. The dust parameterizations of DeMott et al. (2015) (D15) [44] were consistent with our airborne in situ measurements for addressing immersion/condensation freezing at $T > -35$ °C [12] and deposition nucleation parameterization at $T < -33$ °C [43]. It was thus demonstrated that this INP parameterization scheme could provide a trustworthy estimation of dust INP number concentrations from immense D15 and deposition nucleation through the Ullrich et al. (2017) (U17) pathway of dust [42] and the DeMott et al. (2010) [45] (D10) parameterizations of all aerosols [46]. When the SS rate caused by the updraft velocity is in the interval of 0.4–1%, the CCN number concentration is easily increased by 2–3 times [47]. The CCN concentration during dust periods is approximately 2.5 times that in marine periods at an SS of 0.30% [48]. Naturally sourced dust exhibits complex CCN and enhancement factor patterns [49]. Spearman's rank correlation analyses between the CCN and INP number concentrations and the meteorological factors were also performed to examine the effects of atmospheric dynamics on the CCN and INP number concentrations in the presence of various aerosol loadings at Tazhong to better understand the conditions of the desert surface on clouds [50].

We also took measures to retrieve cloud microphysical properties to have a background knowledge of the clouds of this region. The cloud lidar ratio was calculated by combining the cloud optical depth (COD) from the cloud base to the cloud top after diminishing the influence of the multiple scattering effect [51], and the extinction properties of highly turbid atmospheres were derived from Equations (6) and (8) of Ref. [41]. Thus, even uncalibrated lidar could lead to a very stable profile of extinction properties and promptly lose its dependency on the initial estimation of the scattering cross-sections [52]. For simplification, the vertical distribution of the cloud extinction coefficient is calculated by taking the COD into the assumption that there are only clouds and dust in the clouds when clouds appear [53]. Profiles of the effective droplet radius (*Re*), the liquid-water content (*LWC*), liquid-water path (*LWP*), and cloud droplet number concentration (*N_C*) were retrieved based on the following equations:

$$d_{COD} = C \int Re^2 dz \tag{6}$$

$$LWC_Z = \frac{4}{3} \pi \rho_w N_C k Re^3 \tag{7}$$

$$LWP = \int_{Z_{top}}^{Z_{base}} LWC_Z dz \tag{8}$$

where $C = \pi N_C k Q_{ext}$ represents a constant for every layer, N_C is the cloud droplet number concentration, $k = 0.67$ for continental stratocumulus clouds, $Q_{ext} \approx 2$ is applied, and $\rho_w = 1$ g/cm^3 is taken as the water density [54]. CloudSat represents a satellite remote sensing global survey of cloud profiles and cloud physical properties [55]. In this paper, we made use of the *Re*, *LWC*, and *LWP* values of the 2B-CWC-RO product (https://www.cloudsat.cira.colostate.edu/data-products/2b-cwc-ro, (accessed on 1 July 2022)) to present a long time series overview of the conditions of Tazhong clouds and the surrounding areas.

3. Results and Discussion

Five cases of precipitation-causing clouds with heights of approximately 4 km were observed in Tazhong. During the experiments, 829 non-precipitation clouds were also observed, including 638 ice clouds and 189 water clouds. The average cloud top and bottom heights were 8.28 km and 7.05 km, respectively, with an average cloud thickness of 1.23 km over the study region. The mean cloud-to-lidar ratio was observed to be 28 sr, as evaluated based on the identification of cloud and dust cases among all effective observations given

in Ref. [56]; the mean *COD*, *LWC*, and *LWP* values were set to 0.005, 280 mg/m^3, and 239.74 g/m^2, respectively. The 11-year vertical distributions of the *Re* and *LWC* were stratified by 4 km from July 26–30, 2007–2018 (no data in 2011) based on the CloudSat 2B-CWC-RO products, while the aerosol–cloud interactions covered almost the whole range from 0 (no aerosol–cloud interactions) to 1 (linear increase in interactions with aerosol loading) [54], as aerosols are usually associated with multiple environmental factors.

3.1. Polarization Lidar Photometer Networking Conversion Factors over Tazhong

Particles with a radius of 100 nm are considered to be the best-suited CCN reservoir according to a previous research work on a case of desert dust [35] with $c_{100,d}$ = 5.86 cm^{-3} for x_d = 2.73 and σ_d = 1 Mm^{-1}. The number concentrations of particles with dry radii greater than 250 nm were employed in the INP parameterizations as inputs; these number concentrations agreed well (<30–50% deviation) with aircraft measurements taken in the Saharan Air Layer over Barbados [46]. The dust extinction-to-number concentration with a dry radius of more than 250 nm conversion factor ($c_{250,d}$ = 0.20 Mm cm^{-3}) in Tazhong was selected based on the 37 effective observations of Asian dust defined AE < 0.25 and AOD > 0.35 that were identified during 2019, as are presented in Figure 2. The conversion factor was higher than $c_{250,d}$ = 0.19 ± 0.05 Mm cm^{-3} in Wuhan [57], and $c_{280,d}$ = 0.673 Mm cm^{-3} in the Sahara region [58], which indicated that the number concentrations of dust particles in source region, such as the Taklimakan Desert and the Sahara region, was generally higher than those far away from the source area. The extinction-to-volume conversion coefficient, $c_{v,d}$ = 0.85 × 10^{-12} Mmm^3 m^{-3}, was greater than those of the Lanzhou SOCAL station (0.77 × 10^{-12}Mm) and Wuhan (0.52 ± 0.12 × 10^{-12} Mmm^3 m^{-3}) [57]. This issue suggests that the proportion of dust particles in the atmospheric column is relatively coarse in Tazhong.

3.2. Vertical Distribution of Clouds, CCN, and INPs in the Presence of Different Pollution Levels

From July 26 to 30, 2019, a total of 22 sounding balloon experiments were conducted, of which three artificial records presented cirrus clouds in the sky and a small amount of floating dust on the ground. The CCN and INP profiles of three pollution levels on the surface and three typical water clouds, mixed-phase clouds, and ice clouds in the atmosphere are illustrated in Figure 3, as the CCN were associated with air mass transport and air masses [59]; in addition, negative relationships between the CCN modality and low-altitude cloudiness have been previously reported [60]. The highest aerosol–cloud interaction values were obtained about 500 m below the cloud base [61]. The INP activity in the range of the Arizona Test Dust processed by the industry is somewhat higher than that of the natural mineral dusts in the Sahara and Canary Islands [62].

The duration of each sounding observation was approximately 1.5 h, while the temporal resolution of the lidar observations was approximately 3 min. The lidar data corresponding to the sounding observation periods were thus selected to evaluate the 532 nm total attenuated backscatter coefficient (TABC) and volume depolarization ratio (VDR) according to the method described in Ref. [36]; then, the average TABC was evaluated at the wavelength of 532 nm during the observation period. The Fernald method was also applied to retrieve the extinction coefficient and substitute the conversion ratio calculated in Section 3.1; then, the CCN and INP profiles in the presence of various parametric modes were achieved, as are discussed in the following subsections.

3.2.1. Water Cloud

Based on radiosonde observations taken on 26 July 2019, the polarization lidar observations manually revealed that the ground was covered with dust storms. The sixth sounding period was selected as the typical cirrus detection time for the analysis, as is demonstrated in Figure 4; in this period, a cirrus water cloud at was detectable at heights of 5.8–6.5 km within most of the sounding time range. The average PM$_{10}$ and PM$_{2.5}$ values during this sounding period were 481.7 µg m^{-3} and 85.5 µg m^{-3}, respectively, with

a ratio ($PM_{10}/PM_{2.5}$) of 5.67, which reflected the air pollution conditions and pollution sources [63].
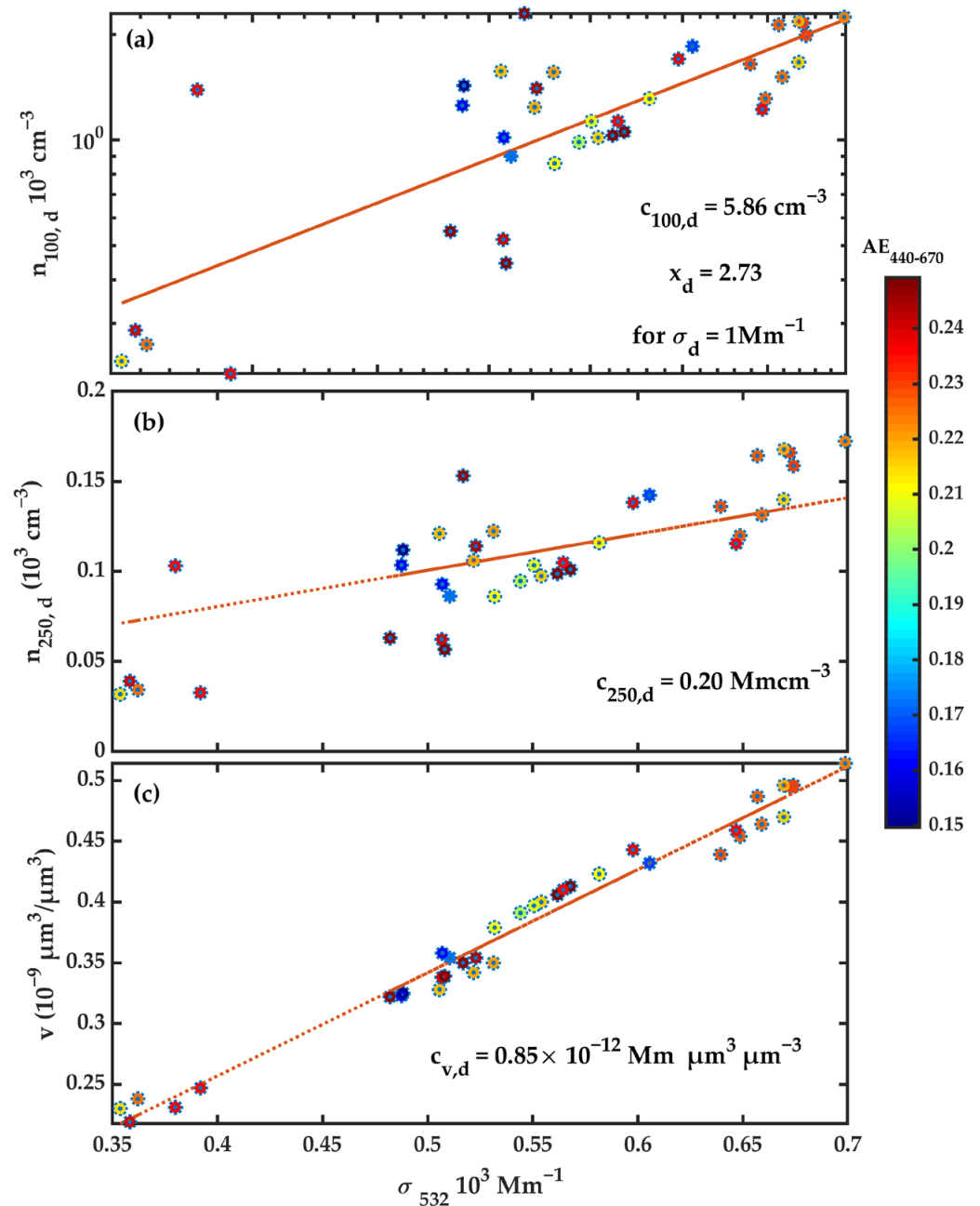
Figure 3. Relationship between the average dust layer extinction coefficient σ_{532nm} for (**a**) dust column number concentrations $n_{100,d}$, (**b**) $n_{250,d}$ and (**c**) $c_{v,d}$ for various Ångström exponents (AE) shown with the color bar on the right side in Tazhong.

The wind direction below 3 km rotated counterclockwise in terms of the height (not shown here), and a strong cold advection surface cold front was passing through the study area, where cold air and cyclones related to springtime frontal dust storms are common [64]. The front moved from north to south, and an area of atmospheric instability could be observed in the northeastern direction. The results plotted in Figure 5b indicate that the *Vel* from the ground to a height of 9 km generally presented a fluctuating upward trend. This fluctuation was weak within the cloud, and was noticeable at the cloud bottom and cloud top. Both the cloud bottom and the cloud top *Vel* rose. According to the wind direction variations, it was judged that cold advection existed at the cloud bottom, and a warm

advection existed at the cloud top. The CCN number concentration varied from 10^{-5} L^{-1} to 10^3 L^{-1}, and the CCN concentration in the cloud reached 10^2 L^{-1}. Figure 5b shows that the INP concentration varied between 10^{-2} L^{-1} and 10^1 L^{-1}. In the stratocumulus layer, at the top of the convective boundary layer, the cloud droplet number concentration and CCN number concentration (for 0.2% water SS) values ranged from 15–100 to 75–200 cm^{-3} during updraft periods recording by radiosonde observations, respectively, and the highest aerosol–cloud interaction values were obtained when considering aerosol proxies measured at heights approximately 500 m below the cloud base [61]. At altitudes of 7.5–8.8 km, INP parameterization schemes D10 and D15 were applicable, where INP concentrations obtained with parameterization schemes D15 were more than INP concentrations obtained with parameterization schemes D10 at above 9 km in height. There was a temperature inversion layer at heights of 2–2.3 km and 6.2–6.6 km at the cloud top, with an average thickness of approximately 0.35 km. The graphs depicted in Figure 5c,d reveal that, at 5.6–6.5 km where the cloud layer was located, the RH and dew point temperature were considerably magnified and reached 84% and −18 °C, respectively; thus, the water vapor content was sufficient, the cloud consisted mostly of liquid water, and the cloud top temperature was −15.63 °C.
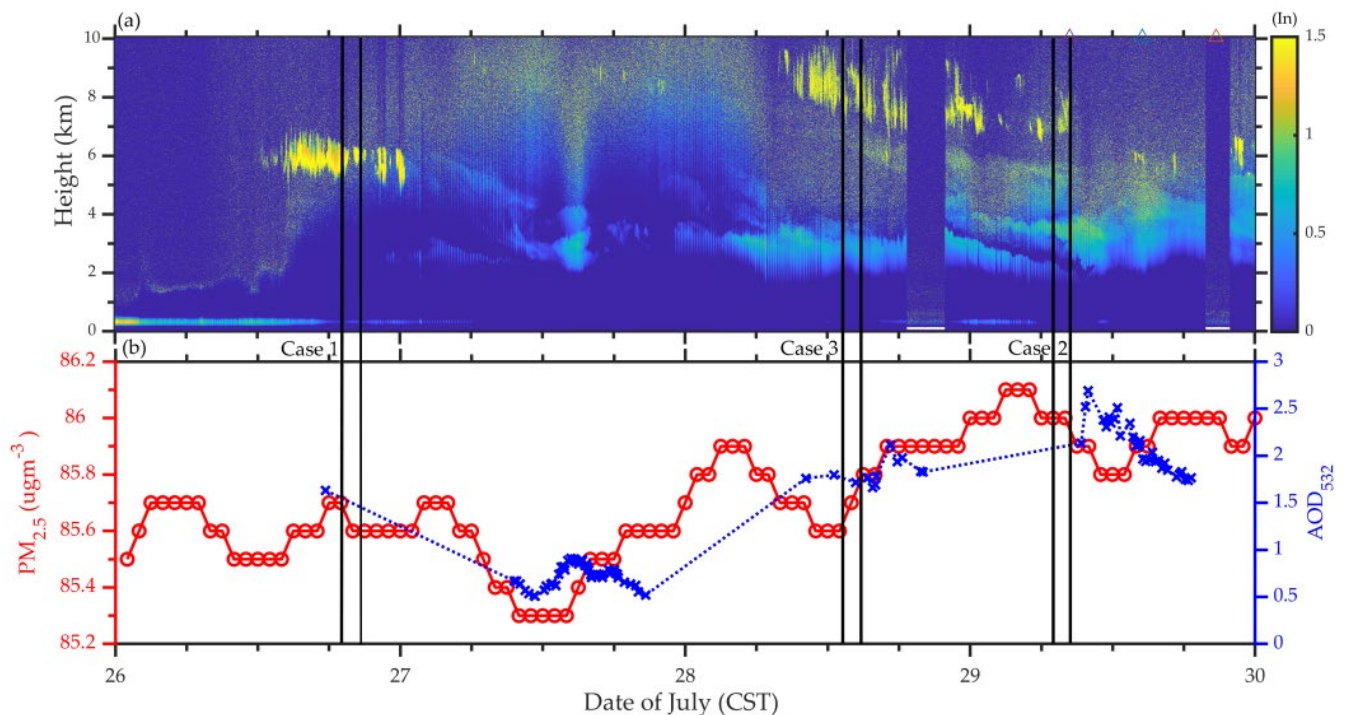

Figure 4. (**a**) Variations in color ratio (1064 nm/532 nm) obtained from lidar measurements and (**b**) PM$_{2.5}$ and AOD values recorded from 26–30 July 2019.

3.2.2. Mixed Cloud

On 29 July 2022, a total of four sounding observations were conducted. The ground-recorded observations showed a sunny day, a small amount of floating dust on the surface, and a small amount of cirrus clouds in the sky; the PM$_{10}$ and PM$_{2.5}$ concentrations in the second observation period were 783.39 µg m^{-3} and 86 µg m^{-3}, respectively. The PM$_{10}$/PM$_{2.5}$ value was 9.1, and the average AOD was observed to be 0.24.

The wind direction below 3 km rotated anticlockwise as a function of height, and a strong cold advection surface cold front was passing through. The front moved from northwest to southeast, and an area of atmospheric instability existed in the east–west direction. In combination with the large TABC change with time during the sounding period, as is shown in Figure 6c,d, the vertical profile of the TABC after averaging showed a large fluctuation, thus resulting in a large fluctuation in the vertical CCN profile calculated

by the inverse extinction coefficient, as is shown in Figure 6a. Figure 6a displays that the CCN concentrations varied from 10^{-5} L^{-1} to 0.5 L^{-1} above 4 km and higher than 0.55 L^{-1} below 4 km; such discrepancies may be attributed to the fact that the droplet number is sensitive to the change in both aerosol concentration and vertical velocity and is limited to 150–550 cm^{-3} in mixed-phase clouds [65]. The results displayed in Figure 6b reveal that the INP concentration varied in the range of 10^{-3}–1 L^{-1} in Tazhong, which is comparable to the concentration of 0.01–1 L^{-1} in Dushanbe at the 6–8 km height range under mixed-phase cloud conditions in spring and summer, which may be due to their homologous dust [34]. The maximum value of this concentration was lower than the maximum value between 0.18–12.4 L^{-1}, 0.39–24 L^{-1}, and 1.1–40.2 L^{-1} measured over a high-altitude station in the Western Ghats, India [31]. That may be the result because feldspar particles in the Tazhong area are lower than that in India, because feldspar particles are the main component of dust ice nuclei at temperatures below about -15 °C [66], and super micron particles contribute to more than half of the INP concentrations at warmer than -12 °C at higher altitudes [45]. At heights of 7.3–7.9 km, the INP number concentration under parameterization schemes D10 and D15 were applicable, where INP concentrations obtained with D15 were more than INP concentrations obtained with D10 above cloud top height. Figure 6c,d demonstrate that a layer of dust existed at a height of 2.4 km above the ground, clouds were present at heights of 4–5.5 km and 6.5–9 km, and the *Vel* at the cloud top and bottom grew. Figure 6e shows temperature inversion layers at heights of 2–2.2 km and 5.7–6.1 km, with an average thickness of approximately 0.3 km. The RH in the clouds reached 88%, and the dew point temperature was -20 °C. The cloud top temperature was -26.3 °C, as is shown in Figure 6e; below -20 °C, water vapor reaches supersaturation and begins to form ice crystals. Figure 6f indicates that the *Vel* fluctuated in the interval of 0–3.5 km, lessened in the range of 3.5–5 km (to a value of 5 m/s), and grew at 5–10 km (to a value of 22 m/s).
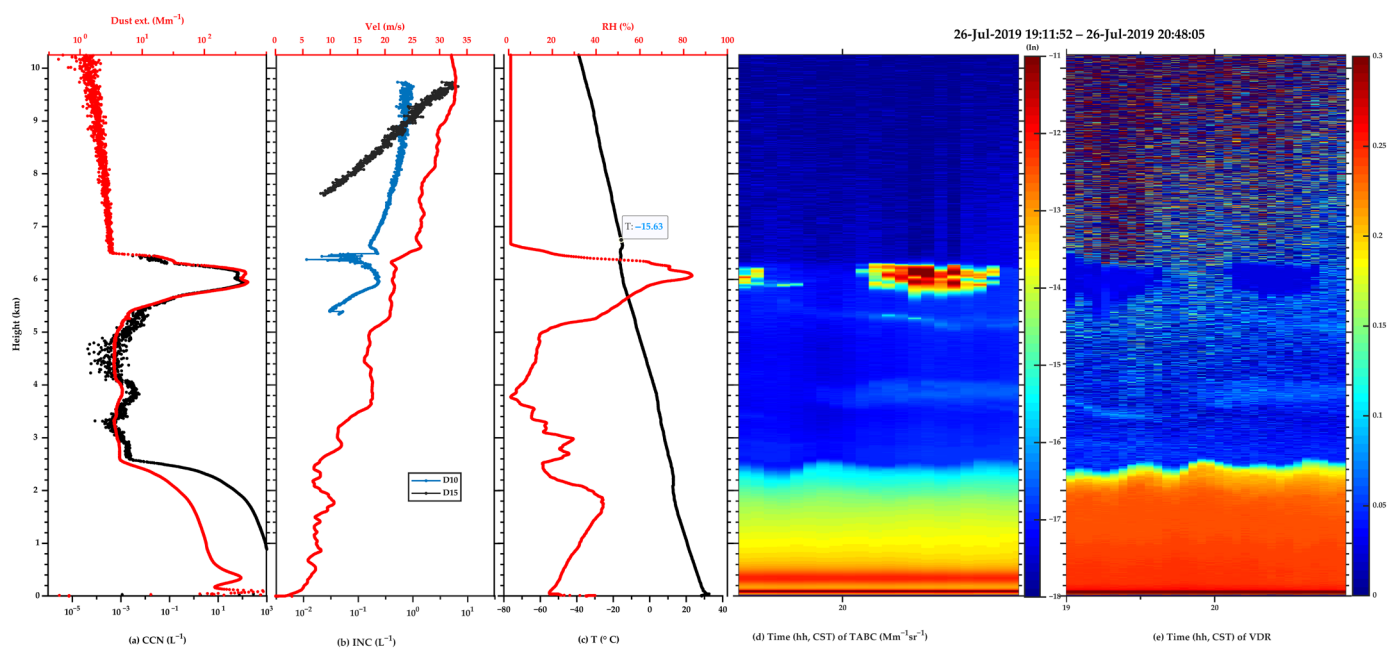
Figure 5. (**a**) Lidar-derived CCN number concentration (unit: cm^{-3}) at 0.2% SS (black pot) with the secondary axis of the red solid line representing the dust extinction coefficient (Dust ext., unit: Mm^{-1}), (**b**) INP number concentration (unit: L^{-1}) profiles with colors specifying various INP parameterization schemes D10 and D15, while the secondary axis of the red solid line represents the wind speed (*Vel*, unit: m/s), (**c**) temperature (*T*, unit: °C) with the marking point as cloud top temperature and the secondary axis of the red solid line representing the relative humidity (*RH*, unit: %), (**d**) temporal (Chinese Standard Time) height of TABC$_{532}$, and (**e**) temporal height of VDR$_{532}$.
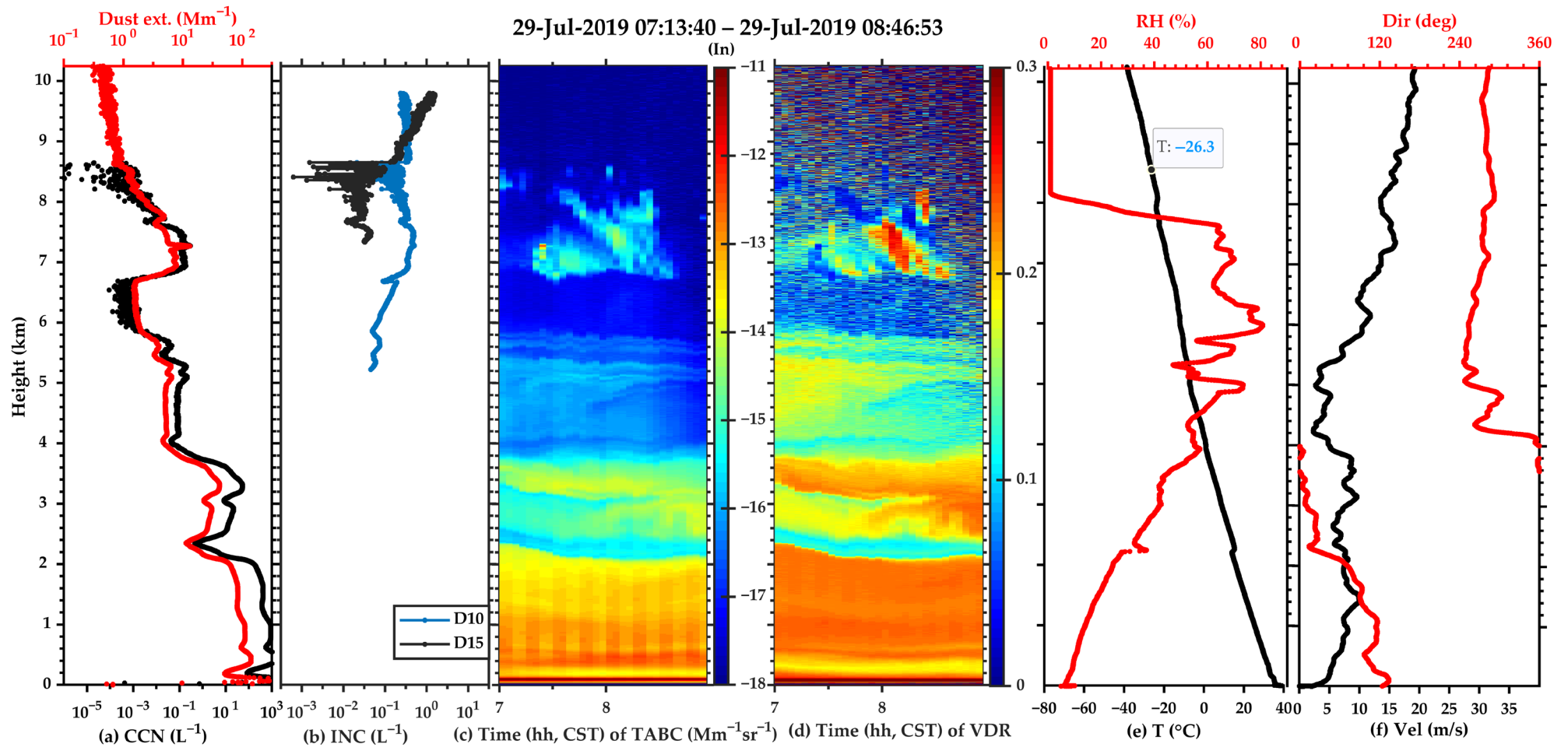
Figure 6. (**a**) Lidar-derived CCN number concentration at 0.2% SS (black pot) with the secondary axis of the red solid line representing the dust extinction coefficient (Dust ext., unit: Mm^{-1}), (**b**) INP number concentration profiles with colors referring to INP parameterization schemes D10 and D15; (**c**) $TABC_{532}$, (**d**) VDR_{532}, (**e**) temperature (*T*, unit: °C) shown in the black line with the marking point as cloud top temperature and RH (unit:%) shown in the red line, and (**f**) wind direction (Dir, unit: °) shown in the red line and *Vel* (unit: m/s) shown in the black line within the sounding time range shown in the title of the figure.

The CCN is easily affected by its source, including the upward transportation of aerosols from the surface [59]. Compared to the dust situation on 26 July 2019, the CCN and INP concentrations of dust in the clear sky were relatively high. The VDR of the dust at heights of 0–1.8 km was approximately 0.28, which was greater than that of fugitive dust (0.21) at heights of 1.4–2.8 km. In the transportation process downward and upward, dust is exposed to wind erosion and is more spherical in shape with the VDR decrease shown.

3.2.3. Ice Cloud

On 28 July 2022, a total of four sounding observations were performed, and a sunny day with small amounts of floating dust and cirrus clouds was appropriately recorded on the ground in the manual record. The PM_{10} and $PM_{2.5}$ concentrations in the second observation period were 408.68 μg m^{-3} and 85.7 μg m^{-3}, respectively, with a $PM_{10}/PM_{2.5}$ value of 4.77 and an average AOD of 0.16.

The wind direction below 1–1.4 km clearly rotated clockwise with height (not shown here), and a warm advection surface front was passing through. The front faced west to east, and an area of atmospheric instability occurred in the western direction. The results illustrated in Figure 7a indicate that the CCN concentration varied from 10^{-1} to 10^5 L^{-6}, and the CCN concentration in the cloud reached about 10^3 L^{-1}. The dew point temperature decreased from the ground to a height of 6 km, and the dew point temperature grew at a height of 6.8–9.4 km within the cloud layer; thus, the water vapor content increased. Figure 7b demonstrates that the INP concentration varied between 0.03 and 10^1 L^{-1}. This INP concentrations was high enough in this height to significantly affect ice formation in ice and mixed-phase clouds [34]. In the height range of 7.2–8.7 km, INP parameterization schemes D10 and D15 were employed, in which the INP concentration in parameterization scheme D15 was more than in the parameterization scheme at above the mid height of the cloud. This means that the parameterization scheme D15 could derive more INP concentrations at low temperatures than the parameterization scheme D10. The *Vel* in the 0.5–8.6 km range displayed a fluctuating upward trend overall. This fluctuation was weak in the cloud and noticeable at the cloud bottom and cloud top. Both the cloud bottom and cloud top rose. Figure 7c,d illustrate that, at heights of 6.8–9.5 km where the cloud layer was located, the RH and dew point temperature substantially increased; the maximum RH was 45%, and the dew point temperature was −32 °C. The cloud was composed mainly of ice crystals, with the cloud top temperature at −58.7 °C.

3.3. Effects of Atmospheric Dynamics on the CCN and INPs in the Hinterland of the Taklimakan Desert during the Summer of 2019

Previous lidar observations have indicated that strong aerosol–cloud interactions occur during updraft periods [67]. The *Vel* in the 5–15-km range illustrated an ascending trend with increasing height and a descending trend from 15 km to 20 km, while this term showed an ascending trend with increasing height from 20 km to 30 km. In the height interval of 15–20 km, the *Vel* was greater than 30 m/s, thus forming a westerly upper air jet [68]. In the height range of approximately 5–17 km from the top of the troposphere to the bottom of the stratosphere, the *Vel* direction was mostly westerly. However, the *Vel* direction was easterly at heights of approximately 21–30 km. The wind directions of the lower and upper layers were opposite, and the middle atmosphere flowed to the lower and upper layers, thus separating them. This could be the reason that the airborne Asian dust stable layer formed but did not spread to the ground with the long-term existence of the stagnant layer in the desert hinterland of Tazhong [69]. During the 22 sounding observation periods considered herein, 19 effective lidar observations were performed. The data density distributions and box diagrams of the WS and INP in the parameterization scheme D10, RH, and 1.125–3.75-km CCN are presented in Figure 8.
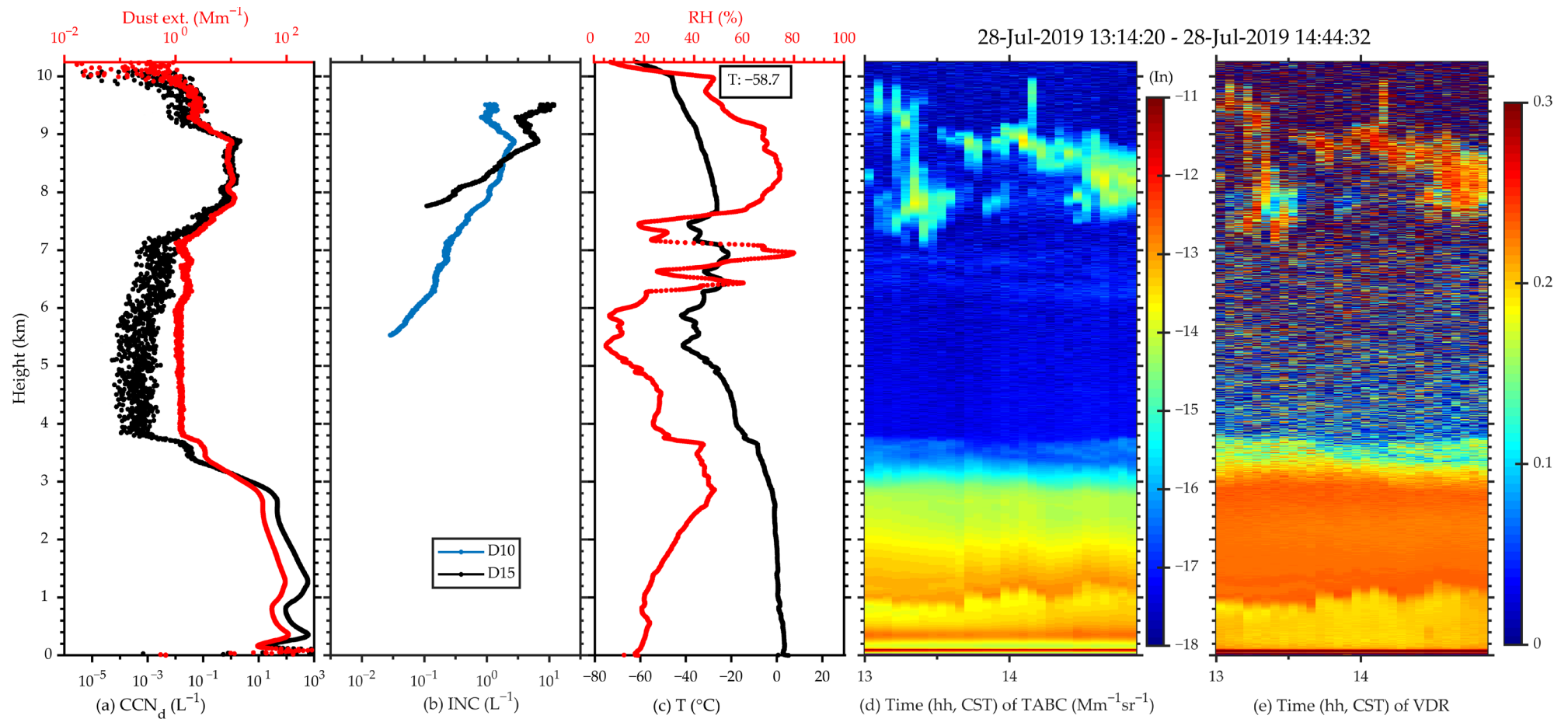
Figure 7. (**a**) Lidar–derived CCN number concentration at 0.2% SS (black pot) with the secondary axis of the red solid line representing the dust extinction coefficient (Dust ext., unit: Mm^{-1}), (**b**) INP number concentration profiles with colors referring to INP parameterization schemes D10 and D15; (**c**) temperature (*T*, unit: °C) shown in the black line with the marking point as cloud top temperature and the secondary axis of *RH* (unit: %) shown in the red line, (**d**) temporal height of $TABC_{532}$, and (**e**) temporal height of VDR_{532}.
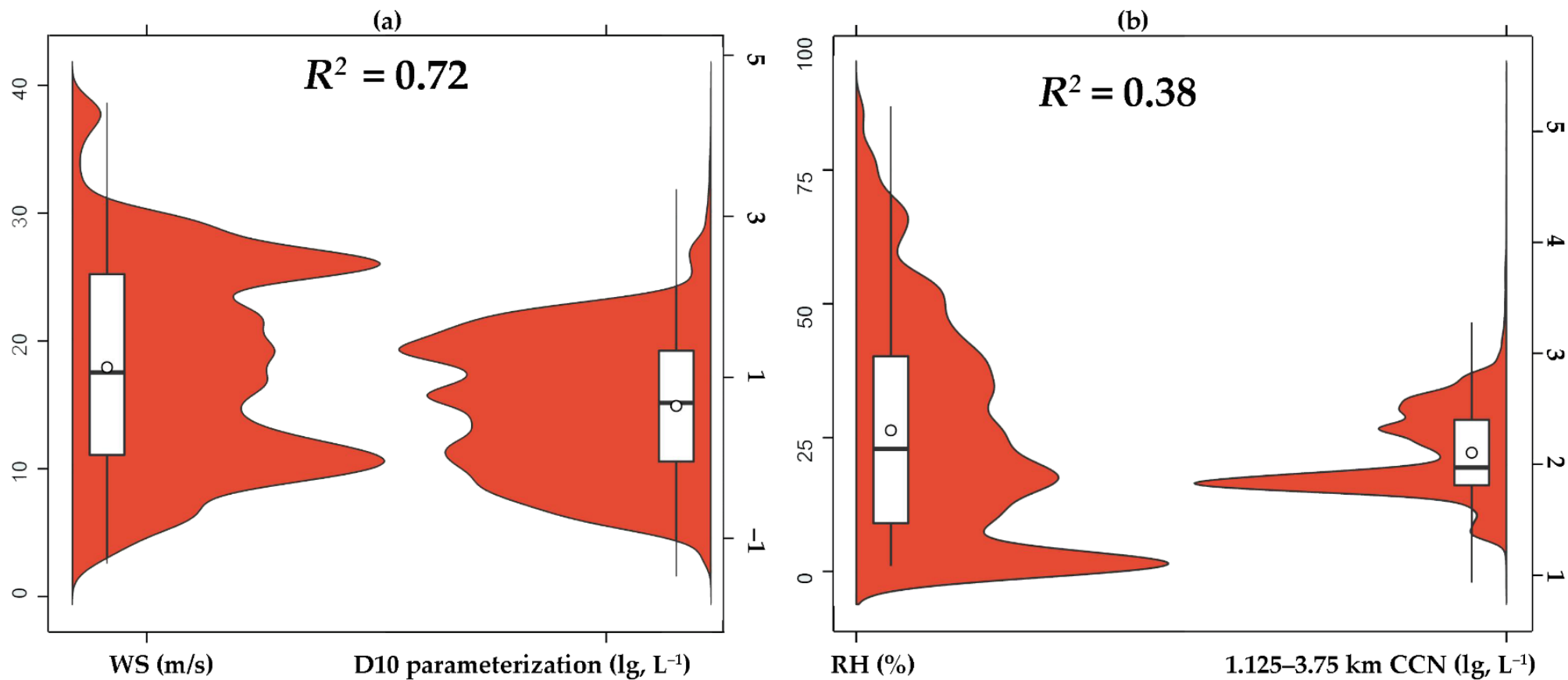
Figure 8. Spearman's rank correlation coefficients between the INP in parameterization scheme D10 and WS are shown in (**a**), and the 1.125–3.75-km CCN and RH are shown in (**b**). The y-axis is the data value, and the x-axis is the probability density of the data.

When calculating the correlation coefficients between the CCN and meteorological elements, considering that CCNs below 1 km and above 4 km are greatly affected by ground dust and other forms of clouds in the upper air, respectively, the height range of 1.125–3.75 km was finally selected in combination with the vertical resolution of the lidar data, and relatively natural CCN and meteorological elements were selected for the correlation analysis. The CCN and INP number concentrations in the height range of 10–12 km input to parameterization schemes D10 and D15 and to the normal distributions of the CCN and INP number concentrations in the parameterization scheme D10, which varied in the intervals 10^{-2}–10^{2} L^{-1} and 10^{-2}–10^{4} L^{-1}, while the INP number concentrations applied in the parameterization scheme D15 varied from 10^{-2} to 10^{4} L^{-1}. The CCN number concentration decreased from the ground to a height of 12 km, with an average value of 36.57 L^{-1}, an upper quartile of 19.71 L^{-1}, and a final quartile of 49.47 L^{-1}, which was much higher than the CCNs at 0.2% SS, which fell mostly in the range of 994 to 6268 cm^{-3} in the foggy/hazy and clear cases of Shanghai [70] and of 3 to 590 cm^{-3} during the Antarctic Circumnavigation Expedition (ACE) [71]. Such discrepancies could be attributed to the fact that the particle concentration in the desert is higher than that in the seaside and Antarctic. The CCNs at heights below 4 km were substantially higher than those above 4 km, which was consistent with the observation that clouds below 4 km easily form precipitation. The INP number concentration under the parameterization scheme D10 had a mean value of 3.50 L^{-1}, while the upper and last quartiles were 0.97 L^{-1} and 21.44 L^{-1}; among the parameterization schemes, D15 had a mean value of 7.80 L^{-1} at 0.15% SS. In the Saharan air layer, the CCNs were 100–300 cm^{-3} at 0.2% SS and the INPs were 10–200 L^{-1} at 25 °C over the Barbados region [46], which were lower than values between 0.7 and 1.5×10^{9} CCN m^{-3} at 0.2% SS [72]. The vertical distribution of the INP number concentration under various modes presented a decreasing trend with height, and clouds or the ground dust concentration exhibited pronounced impacts on the CCN and INP number concentrations [73]. The INP number concentration under the D10 mode was greater than that under the D15 mode. The Spearman's rank correlation coefficient values between D10 and *Vel* were 0.72 and 0.38 for CCN and RH, respectively, which were within the height range of 1.125–3.75 km. These results show that sounding balloon observations provided more possibilities for cloud microphysics parameterization schemes. At the same time, the importance of sounding balloon observation was emphasized.

4. Conclusions

The number concentrations of the CCN and INP number concentrations in the hinterland of the Taklimakan Desert were analyzed in this study for the first time regarding the temperature and pressure profiles combined with meteorological data observed using a sounding balloon and dust data based on lidar and a sun photometer. As the extinction coefficient was noticeably influenced by dust on the ground and clouds at high altitudes, this methodology was applied by considering the concentrations of CCN and INP in the presence of different pollution intensities and cloud conditions and then selecting typical cases for analysis. Based on the function of lidar in distinguishing different components of atmospheric particles, this work confirms the value of lidar combined with meteorological data in daily observation.

The results indicated that the dust in the Tazhong area is coarser than that in other areas farther from the dust source (such as Lanzhou and Wuhan), and the dust number concentrations are higher and support previous investigations of aerosol–cloud–precipitation interactions performed in desert areas. The achieved results reveal that the CCN and INP number concentrations spanned four orders of magnitude and were substantially affected by dust below 4 km [74] and by clouds at high altitudes; this could have been due to dust and clouds providing increased CCN and INPs by acting as CCN and INPs, which thus emphasize the importance of considering dust and clouds in CCN and INP parameterization schemes. When the CCN was dominated by dust particles, it produced changes in the ice cloud particle size and concentration and was responsible for starting

drizzling and precipitation in special meteorology–aerosol connections. The correlations between atmospheric dynamics and the CCN and INP values in desert regions due to various cloud conditions and pollution levels highlighted the significance of exploring meteorology–aerosol–cloud connections alongside the correlations between the ecological environment and CCN or INP, which requires further assessment.

Author Contributions: S.Z. carried out the data collection, initial analysis, and drafted the initial manuscript under the guidance of Z.H. and K.A.; the sounding data were collected by J.Z., W.W., and Z.C.; the sun photometer data were provided by J.B.; M.L., X.S. (Xingtai Shen), Q.D., Y.W., W.L., Z.L., and X.S. (Xiaodong Song) contributed to the lidar maintenance and data collection. All authors have read and agreed to the published version of the manuscript.

Data Availability Statement: Not applicable.

Conflicts of Interest: The authors declare no conflict of interest.

References

1. Zhang, Z.; Zhou, W.; Wenig, M.; Yang, L. Impact of Long-Range Desert Dust Transport on Hydrometeor Formation over Coastal East Asia. *Adv. Atmos. Sci.* **2017**, *34*, 101–115. [CrossRef]
2. Hoose, C.; Lohmann, U.; Erdin, R.; Tegen, I. The Global Influence of Dust Mineralogical Composition on Heterogeneous Ice Nucleation in Mixed-Phase Clouds. *Environ. Res. Lett.* **2008**, *3*, 25003. [CrossRef]
3. Kelly, J.T.; Chuang, C.C.; Wexler, A.S. Influence of Dust Composition on Cloud Droplet Formation. *Atmos. Environ.* **2007**, *41*, 2904–2916. [CrossRef]
4. Barahona, D.; West, R.E.L.; Stier, P.; Romakkaniemi, S.; Kokkola, H.; Nenes, A. Comprehensively Accounting for the Effect of Giant CCN in Cloud Activation Parameterizations. *Atmos. Chem. Phys.* **2010**, *10*, 2467–2473. [CrossRef]
5. Lee, Y.H.; Chen, K.; Adams, P.J. Development of a Global Model of Mineral Dust Aerosol Microphysics. *Atmos. Chem. Phys.* **2009**, *9*, 2441–2458. [CrossRef]
6. Manktelow, P.T.; Carslaw, K.S.; Mann, G.W.; Spracklen, D.V. The Impact of Dust on Sulfate Aerosol, CN and CCN during an East Asian Dust Storm. *Atmos. Chem. Phys.* **2010**, *10*, 365–382. [CrossRef]
7. Orikasa, N.; Saito, A.; Yamashita, K.; Tajiri, T.; Zaizen, Y.; Kuo, T.H.; Kuo, W.C.; Murakami, M. Seasonal Variations of Atmospheric Aerosol Particles Focused on Cloud Condensation Nuclei and Ice Nucleating Particles from Ground-Based Observations in Tsukuba, Japan. *Sci. Online Lett. Atmos.* **2020**, *16*, 212–219. [CrossRef]
8. Zhang, Y.; Yu, F.; Luo, G.; Fan, J.; Liu, S. Impacts of Long-Range-Transported Mineral Dust on Summertime Convective Cloud and Precipitation: A Case Study over the Taiwan Region. *Atmos. Chem. Phys.* **2021**, *21*, 17433–17451. [CrossRef]
9. Uetake, J.; Hill, T.C.J.; Moore, K.A.; DeMott, P.J.; Protat, A.; Kreidenweis, S.M. Airborne Bacteria Confirm the Pristine Nature of the Southern Ocean Boundary Layer. *Proc. Natl. Acad. Sci. USA* **2020**, *117*, 13275–13282. [CrossRef]
10. Ziemba, L.D.; Beyersdorf, A.J.; Chen, G.; Corr, C.A.; Crumeyrolle, S.N.; Thornhill, K.L.; Winstead, E.L.; Wisthaler, A.; Anderson, B.E. Airborne Observations of Bioaerosol over the Southeast United States Using a Wideband Integrated Bioaerosol Sensor. *J. Geophys. Res. Atmos.* **2016**, *16*, 8506–8524. [CrossRef]
11. Gong, X.; Wex, H.; Müller, T.; Wiedensohler, A.; Höhler, K.; Kandler, K.; Ma, N.; Dietel, B.; Schiebel, T.; Möhler, O.; et al. Characterization of Aerosol Properties at Cyprus, Focusing on Cloud Condensation Nuclei and Ice-Nucleating Particles. *Atmos. Chem. Phys.* **2019**, *19*, 10883–10900. [CrossRef]
12. Schrod, J.; Weber, D.; Drücke, J.; Keleshis, C.; Pikridas, M.; Ebert, M.; Cvetković, B.; Nickovic, S.; Marinou, E.; Baars, H.; et al. Ice Nucleating Particles over the Eastern Mediterranean Measured by Unmanned Aircraft Systems. *Atmos. Chem. Phys.* **2017**, *17*, 4817–4835. [CrossRef]
13. Xi, Y.; Xu, C.; Downey, A.; Stevens, R.; Bachelder, J.O.; King, J.; Hayes, P.L.; Bertram, A.K. Ice Nucleating Properties of Airborne Dust from an Actively Retreating Glacier in Yukon, Canada. *Environ. Sci. Atmos.* **2022**, *2*, 714–726. [CrossRef]
14. Paramonov, M.; Paramonov, M.; Van Dusseldorp, S.D.; Gute, E.; Abbatt, J.P.D.; Heikkilä, P.; Keskinen, J.; Chen, X.; Chen, X.; Luoma, K.; et al. Condensation/Immersion Mode Ice-Nucleating Particles in a Boreal Environment. *Atmos. Chem. Phys.* **2020**, *20*, 6687–6706. [CrossRef]

15. Li, J.; Liu, W.; Castarède, D.; Gu, W.; Li, L.; Ohigashi, T.; Zhang, G.; Tang, M.; Thomson, E.S.; Hallquist, M.; et al. Hygroscopicity and Ice Nucleation Properties of Dust/Salt Mixtures Originating from the Source of East Asian Dust Storms. *Front. Environ. Sci.* **2022**, *10*, 897127. [CrossRef]

16. Rinaldi, M.; Hiranuma, N.; Santachiara, G.; Mazzola, M.; Mansour, K.; Paglione, M.; Rodriguez, C.A.; Traversi, R.; Becagli, S.; Cappelletti, D.; et al. Ice-Nucleating Particle Concentration Measurements from Ny-Ålesund during the Arctic Spring-Summer in 2018. *Atmos. Chem. Phys.* **2021**, *21*, 14725–14748. [CrossRef]

17. Huang, J.; Minnis, P.; Lin, B.; Wang, T.; Yi, Y.; Hu, Y.; Sun-Mack, S.; Ayers, K. Possible Influences of Asian Dust Aerosols on Cloud Properties and Radiative Forcing Observed from MODIS and CERES. *Geophys. Res. Lett.* **2006**, *33*, e2005GL024724. [CrossRef]

18. Shinozuka, Y.; Clarke, A.D.; Nenes, A.; Jefferson, A.; Wood, R.; McNaughton, C.S.; Ström, J.; Tunved, P.; Redemann, J.; Thornhill, K.L.; et al. The Relationship between Cloud Condensation Nuclei (CCN) Concentration and Light Extinction of Dried Particles: Indications of Underlying Aerosol Processes and Implications for Satellite-Based CCN Estimates. *Atmos. Chem. Phys.* **2015**, *15*, 7585–7604. [CrossRef]

19. Wang, M.; Xiao, M.; Bertozzi, B.; Marie, G.; Rörup, B.; Schulze, B.; Bardakov, R.; He, X.-C.; Shen, J.; Scholz, W.; et al. Synergistic HNO_3–H_2SO_4–NH_3 Upper Tropospheric Particle Formation. *Nature* **2022**, *605*, 483–489. [CrossRef]

20. Phillips, V.T.J.; Choularton, T.W.; Illingworth, A.J.; Hogan, R.J.; Field, P.R. Simulations of the Glaciation of a Frontal Mixed-Phase Cloud with the Explicit Microphysics Model. *Q. J. R. Meteorol. Soc.* **2003**, *129*, 1351–1371. [CrossRef]

21. Yin, Y.; Levin, Z.; Reisin, T.G.; Tzivion, S. The Effects of Giant Cloud Condensation Nuclei on the Development of Precipitation in Convective Clouds—A Numerical Study. *Atmos. Res.* **2000**, *53*, 91–116. [CrossRef]

22. Yang, H.L.; Xiao, H.; Hong, Y.C. The Effects of Giant Cloud Condensation Nuclei on the Structure of Precipitation in Hailstorm Clouds. *Sci. China Earth Sci.* **2012**, *55*, 126–142. [CrossRef]

23. He, Q.; Li, H.; Li, X.; Yang, Q.; Pan, X.; Gao, W. Preliminary Analysis on Boundary Climate Effects between Oasis and Desert in the North Margin of the Taklimakan Desert. *Remote Sens. Model. Ecosyst. Sustain.* **2004**, *5544*, 448. [CrossRef]

24. Yang, Y.; Zhao, C.; Han, M.; Li, Y.; Yang, R. Temporal Patterns of Shrub Vegetation and Variation with Precipitation in Gurbantunggut Desert, Central Asia. *Adv. Meteorol.* **2015**, *2015*, 23–27. [CrossRef]

25. Yang, P.; Zhao, L.; Liang, X.; Niu, Z.; Zhao, H.; Wang, Y.; Wang, N. Response of Net Ecosystem CO_2 Exchange to Precipitation Events in the Badain Jaran Desert. *Environ. Sci. Pollut. Res.* **2022**, *29*, 36486–36501. [CrossRef]

26. Li, G.; Yang, H.; Zhang, Y.; Huang, C.; Pan, X.; Ma, M.; Song, M.; Zhao, H. More Extreme Precipitation in Chinese Deserts From 1960 to 2018. *Earth Planets Space* **2019**, *6*, 1196–1204. [CrossRef]

27. Naidoo, Y.; Valverde, A.; Pierneef, R.E.; Cowan, D.A. Differences in Precipitation Regime Shape Microbial Community Composition and Functional Potential in Namib Desert Soils. *Microb. Ecol.* **2022**, *83*, 689–701. [CrossRef]

28. Salguero-Gómez, R.; Siewert, W.; Casper, B.B.; Tielbörger, K. A Demographic Approach to Study Effects of Climate Change in Desert Plants. *Philos. Trans. R. Soc. B Biol. Sci.* **2012**, *367*, 3100–3114. [CrossRef]

29. Ma, N.; Wang, N.; Zhao, L.; Zhang, Z.; Dong, C.; Shen, S. Observation of Mega-Dune Evaporation after Various Rain Events in the Hinterland of Badain Jaran Desert, China. *Chin. Sci. Bull.* **2014**, *59*, 162–170. [CrossRef]

30. Glassmeier, F.; Possner, A.; Vogel, B.; Vogel, H.; Lohmann, U. A Comparison of Two Chemistry and Aerosol Schemes on the Regional Scale and the Resulting Impact on Radiative Properties and Liquid- and Ice-Phase Aerosol-Cloud Interactions. *Atmos. Chem. Phys.* **2017**, *17*, 8651–8680. [CrossRef]

31. Kumar, V.A.; Pandithurai, G.; Kulkarni, G.; Hazra, A.; Patil, S.S.; Dudhambe, S.D.; Patil, R.D.; Chen, J.P.; Niranjan, K. Atmospheric Ice Nuclei Concentration Measurements over a High Altitude-Station in the Western Ghats, India. *Atmos. Res.* **2020**, *235*, 104795. [CrossRef]

32. Burkert-Kohn, M.; Wex, H.; Welti, A.; Hartmann, S.; Grawe, S.; Hellner, L.; Herenz, P.; Atkinson, J.D.; Stratmann, F.; Kanji, Z.A. Leipzig Ice Nucleation Chamber Comparison (LINC): Intercomparison of Four Online Ice Nucleation Counters. *Atmos. Chem. Phys.* **2017**, *17*, 11683–11705. [CrossRef]

33. Zhang, D.; Wang, Z.; Kollias, P.; Vogelmann, A.M.; Yang, K.; Luo, T. Ice Particle Production in Mid-Level Stratiform Mixed-Phase Clouds Observed with Collocated A-Train Measurements. *Atmos. Chem. Phys.* **2018**, *18*, 4317–4327. [CrossRef]

34. Hofer, J.; Ansmann, A.; Althausen, D.; Engelmann, R.; Baars, H.; Abdullaev, S.F.; Makhmudov, A.N. Long-Term Profiling of Aerosol Light Extinction, Particle Mass, Cloud Condensation Nuclei, and Ice-Nucleating Particle Concentration over Dushanbe, Tajikistan, in Central Asia. *Atmos. Chem. Phys.* **2020**, *20*, 4695–4711. [CrossRef]

35. Mamouri, R.E.; Ansmann, A. Potential of Polarization Lidar to Provide Profiles of CCN-and INP-Relevant Aerosol Parameters. *Atmos. Chem. Phys.* **2016**, *16*, 5905–5931. [CrossRef]

36. Zhang, S.; Huang, Z.; Li, M.; Shen, X.; Wang, Y.; Dong, Q.; Bi, J.; Zhang, J.; Li, W.; Li, Z.; et al. Vertical Structure of Dust Aerosols Observed by a Ground-Based Raman Lidar with Polarization Capabilities in the Center of the Taklimakan Desert. *Remote Sens.* **2022**, *14*, 2461. [CrossRef]

37. Dubovik, O.; Herman, M.; Holdak, A.; Lapyonok, T.; Tanré, D.; Deuzé, J.L.; Ducos, F.; Sinyuk, A.; Lopatin, A. Statistically Optimized Inversion Algorithm for Enhanced Retrieval of Aerosol Properties from Spectral Multi-Angle Polarimetric Satellite Observations. *Atmos. Meas. Tech.* **2011**, *4*, 975–1018. [CrossRef]

38. Ma, X.; Huang, Z.; Qi, S.; Huang, J.; Zhang, S.; Dong, Q.; Wang, X. Ten-Year Global Particulate Mass Concentration Derived from Space-Borne CALIPSO Lidar Observations. *Sci. Total Environ.* **2020**, *721*, 137699. [CrossRef]

39. Horvath, H.; Gunter, R.L.; Wilkison, S.W. Determination of the Coarse Mode of the Atmospheric Aerosol Using Data from a Forward-Scattering Spectrometer Probe. *Aerosol Sci. Technol.* **1990**, *12*, 964–980. [CrossRef]

40. Chen, L.; Peng, C.; Gu, W.; Fu, H.; Jian, X.; Zhang, H.; Zhang, G.; Zhu, J.; Wang, X.; Tang, M. On Mineral Dust Aerosol Hygroscopicity. *Atmos. Chem. Phys.* **2020**, *20*, 13611–13626. [CrossRef]

41. Fernald, F.G. Analysis of Atmospheric Lidar Observations: Some Comments. *Appl. Opt.* **1984**, *23*, 652–653. [CrossRef] [PubMed]

42. Marinou, E.; Tesche, M.; Nenes, A.; Ansmann, A.; Schrod, J.; Mamali, D.; Tsekeri, A.; Pikridas, M.; Baars, H.; Engelmann, R.; et al. Retrieval of Ice-Nucleating Particle Concentrations from Lidar Observations and Comparison with UAV in Situ Measurements. *Atmos. Chem. Phys.* **2019**, *19*, 11315–11342. [CrossRef]

43. Ullrich, R.; Hoose, C.; Möhler, O.; Niemand, M.; Wagner, R.; Höhler, K.; Hiranuma, N.; Saathoff, H.; Leisner, T. A New Ice Nucleation Active Site Parameterization for Desert Dust and Soot. *J. Atmos. Sci.* **2017**, *74*, 699–717. [CrossRef]

44. DeMott, P.J.; Prenni, A.J.; McMeeking, G.R.; Sullivan, R.C.; Petters, M.D.; Tobo, Y.; Niemand, M.; Möhler, O.; Snider, J.R.; Wang, Z.; et al. Integrating Laboratory and Field Data to Quantify the Immersion Freezing Ice Nucleation Activity of Mineral Dust Particles. *Atmos. Chem. Phys.* **2015**, *15*, 393–409. [CrossRef]

45. DeMott, P.J.; Prenni, A.J.; Liu, X.; Kreidenweis, S.M.; Petters, M.D.; Twohy, C.H.; Richardson, M.S.; Eidhammer, T.; Rogers, D.C. Predicting Global Atmospheric Ice Nuclei Distributions and Their Impacts on Climate. *Proc. Natl. Acad. Sci. USA* **2010**, *107*, 11217–11222. [CrossRef]

46. Haarig, M.; Walser, A.; Ansmann, A.; Dollner, M.; Althausen, D.; Sauer, D.; Farrell, D.; Weinzierl, B. Profiles of Cloud Condensation Nuclei, Dust Mass Concentration, and Ice-Nucleating-Particle-Relevant Aerosol Properties in the Saharan Air Layer over Barbados from Polarization Lidar and Airborne in Situ Measurements. *Atmos. Chem. Phys.* **2019**, *19*, 13773–13788. [CrossRef]

47. Hu, D.; Wang, Y.; Yu, C.; Xie, Q.; Yue, S.; Shang, D.; Fang, X.; Joshi, R.; Liu, D.; Allan, J.; et al. Vertical Profile of Particle Hygroscopicity and CCN Effectiveness during Winter in Beijing: Insight into the Hygroscopicity Transition Threshold of Black Carbon. *Faraday Discuss.* **2021**, *226*, 239–254. [CrossRef]

48. Van Pinxteren, M.; Wadinga Fomba, K.; Triesch, N.; Stolle, C.; Wurl, O.; Bahlmann, E.; Gong, X.; Voigtländer, J.; Wex, H.; Robinson, T.B.; et al. Marine Organic Matter in the Remote Environment of the Cape Verde Islands-an Introduction and Overview to the MarParCloud Campaign. *Atmos. Chem. Phys.* **2020**, *20*, 6921–6951. [CrossRef]

49. Belosi, F.; Piazza, M.; Nicosia, A.; Santachiara, G. Influence of Supersaturation on the Concentration of Ice Nucleating Particles. *Tellus B Chem. Phys. Meteorol.* **2018**, *70*, 1–10. [CrossRef]

50. Li, J.; Lv, Q.; Zhang, M.; Wang, T.; Kawamoto, K.; Chen, S.; Zhang, B. Effects of Atmospheric Dynamics and Aerosols on the Fraction of Supercooled Water Clouds. *Atmos. Chem. Phys.* **2017**, *17*, 1847–1863. [CrossRef]

51. Chen, W.N.; Chiang, C.W.; Nee, J.B. Lidar Ratio and Depolarization Ratio for Cirrus Clouds. *Appl. Opt.* **2002**, *41*, 6470–6476. [CrossRef] [PubMed]

52. Pal, S.R.; Steinbrecht, W.; Carswell, A.I. Automated Method for Lidar Determination of Cloud-Base Height and Vertical Extent. *Appl. Opt.* **1992**, *31*, 1488. [CrossRef] [PubMed]

53. Tesche, M.; Ansmann, A.; Müller, D.; Althausen, D.; Engelmann, R.; Freudenthaler, V.; Groß, S. Vertically Resolved Separation of Dust and Smoke over Cape Verde Using Multiwavelength Raman and Polarization Lidars during Saharan Mineral Dust Experiment 2008. *J. Geophys. Res. Atmos.* **2009**, *114*, 1–14. [CrossRef]

54. Wang, N.; Zhang, K.; Shen, X.; Wang, Y.; Li, J.; Li, C.; Mao, J.; Malinka, A.; Zhao, C.; Russell, L.M.; et al. Dual-Field-of-View High-Spectral-Resolution Lidar: Simultaneous Profiling of Aerosol and Water Cloud to Study Aerosol-Cloud Interaction. *Proc. Natl. Acad. Sci. USA* **2022**, *119*, e2110756119. [CrossRef] [PubMed]

55. Austin, R.T.; Heymsfield, A.J.; Stephens, G.L. Retrieval of Ice Cloud Microphysical Parameters Using the CloudSat Millimeter-Wave Radar and Temperature. *J. Geophys. Res. Atmos.* **2009**, *114*, 1–19. [CrossRef]

56. Qi, S.; Huang, Z.; Ma, X.; Huang, J.; Shi, J.; Zhou, T.; Zhang, S.; Dong, Q.; Bi, J.; Shi, J. Classification of Atmospheric Aerosols and Clouds by Use of Dual-Polarization Lidar Measurements. *Opt. Express* **2021**, *29*, 23461. [CrossRef]

57. He, Y.; Zhang, Y.; Liu, F.; Yin, Z.; Yi, Y.; Zhan, Y.; Yi, F. Retrievals of Dust-Related Particle Mass and Ice-Nucleating Particle Concentration Profiles with Ground-Based Polarization Lidar and Sun Photometer over a Megacity in Central China. *Atmos. Meas. Tech.* **2021**, *14*, 5939–5954. [CrossRef]

58. Ansmann, A.; Mamouri, R.E.; Hofer, J.; Baars, H.; Althausen, D.; Abdullaev, S.F. Dust Mass, Cloud Condensation Nuclei, and Ice-Nucleating Particle Profiling with Polarization Lidar: Updated POLIPHON Conversion Factors from Global AERONET Analysis. *Atmos. Meas. Tech.* **2019**, *12*, 4849–4865. [CrossRef]

59. Zhang, R.; Wang, Y.; Li, Z.; Wang, Z.; Dickerson, R.R.; Ren, X.; He, H.; Wang, F.; Gao, Y.; Chen, X.; et al. Vertical Profiles of Cloud Condensation Nuclei Number Concentration and Its Empirical Estimate from Aerosol Optical Properties over the North China Plain. *Atmos. Chem. Phys.* **2022**, *22*, 14879–14891. [CrossRef]

60. Hudson, J.G.; Noble, S. Cumulus Cloud and Drizzle Microphysics Relationships With Complete CCN Spectra. *J. Geophys. Res. Atmos.* **2021**, *126*, e2021JD034966. [CrossRef]

61. Jimenez, C.; Ansmann, A.; Engelmann, R.; Donovan, D.; Malinka, A.; Seifert, P.; Wiesen, R.; Radenz, M.; Yin, Z.; Bühl, J.; et al. The Dual-Field-of-View Polarization Lidar Technique: A New Concept in Monitoring Aerosol Effects in Liquid-Water Clouds-Case Studies. *Atmos. Chem. Phys.* **2020**, *20*, 15265–15284. [CrossRef]

62. Roesch, C.; Roesch, M.; Wolf, M.J.; Zawadowicz, M.A.; AlAloula, R.; Awwad, Z.; Cziczo, D.J. CCN and INP Activity of Middle Eastern Soil Dust. *Aeolian Res.* **2021**, *52*, 100729. [CrossRef]

63. Wu, Z.; Wu, X.; Wang, Y.; He, S. PM2.5ĝ•PM10 Ratio Prediction Based on a Long Short-Term Memory Neural Network in Wuhan, China. *Geosci. Model Dev.* **2020**, *13*, 1499–1511. [CrossRef]

64. Shi, L.; Zhang, J.; Yao, F.; Zhang, D.; Guo, H. Drivers to Dust Emissions over Dust Belt from 1980 to 2018 and Their Variation in Two Global Warming Phases. *Sci. Total Environ.* **2021**, *767*, 144860. [CrossRef] [PubMed]

65. Georgakaki, P.; Bougiatioti, A.; Wieder, J.; Mignani, C.; Ramelli, F.; Kanji, Z.A.; Henneberger, J.; Hervo, M.; Berne, A.; Lohmann, U.; et al. On the Drivers of Droplet Variability in Alpine Mixed-Phase Clouds. *Atmos. Chem. Phys.* **2021**, *21*, 10993–11012. [CrossRef]

66. Atkinson, J.D.; Murray, B.J.; Woodhouse, M.T.; Whale, T.F.; Baustian, K.J.; Carslaw, K.S.; Dobbie, S.; O'Sullivan, D.; Malkin, T.L. The Importance of Feldspar for Ice Nucleation by Mineral Dust in Mixed-Phase Clouds. *Nature* **2013**, *498*, 355–358. [CrossRef]

67. Schmidt, J.; Ansmann, A.; Bühl, J.; Wandinger, U. Strong Aerosol-Cloud Interaction in Altocumulus during Updraft Periods: Lidar Observations over Central Europe. *Atmos. Chem. Phys.* **2015**, *15*, 10687–10700. [CrossRef]

68. Uno, I.; Eguchi, K.; Yumimoto, K.; Liu, Z.; Hara, Y.; Sugimoto, N.; Shimizu, A.; Takemura, T. Large Asian Dust Layers Continuously Reached North America in April 2010. *Atmos. Chem. Phys.* **2011**, *11*, 7333–7341. [CrossRef]

69. Tsunematsu, N.; Iwai, H.; Ishii, S.; Yasui, M.; Murayama, Y.; Mizutani, K. Influence of Surface-Based Stable Layer Development on Asian Dust Behaviour over Tokyo. *Bound.-Layer Meteorol.* **2009**, *131*, 263–275. [CrossRef]

70. Leng, C.; Zhang, Q.; Zhang, D.; Xu, C.; Cheng, T.; Zhang, R.; Tao, J.; Chen, J.; Zha, S.; Zhang, Y.; et al. Variations of Cloud Condensation Nuclei (CCN) and Aerosol Activity during Fog-Haze Episode: A Case Study from Shanghai. *Atmos. Chem. Phys.* **2014**, *14*, 12499–12512. [CrossRef]

71. Tatzelt, C.; Henning, S.; Welti, A.; Baccarini, A.; Hartmann, M.; Gysel-Beer, M.; Van Pinxteren, M.; Modini, R.L.; Schmale, J.; Stratmann, F.; et al. Circum-Antarctic Abundance and Properties of CCN and INP. *Atmos. Chem. Phys. Discuss.* **2021**, 1–35, *In review*. [CrossRef]

72. Genz, C.; Schrödner, R.; Heinold, B.; Henning, S.; Baars, H.; Spindler, G.; Tegen, I. Estimation of Cloud Condensation Nuclei Number Concentrations and Comparison to in Situ and Lidar Observations during the HOPE Experiments. *Atmos. Chem. Phys.* **2020**, *20*, 8787–8806. [CrossRef]

73. Kova, N. Sensitivity Study of the Impact of CCN Size on Simulated Ground Precipitation for Deep Convection Case. *Atmos. Environ.* **2022**, *289*, 119309. [CrossRef]

74. Liu, G.; Shao, H.; Coakley, J.A.; Curry, J.A.; Haggerty, J.A.; Tschudi, M.A. Retrieval of Cloud Droplet Size from Visible and Microwave Radiometric Measurements during INDOEX: Implication to Aerosols' Indirect Radiative Effect. *J. Geophys. Res. Atmos.* **2003**, *108*, AAC 2-1–AAC 2-10. [CrossRef]